RSC Advances

PAPER

Cite this: *RSC Adv.*, 2019, **9**, 13088

Microwave absorption enhancement by adjusting reactant ratios and filler contents based on 1D K–MnO$_2$@PDA and poly(vinylidene fluoride) matrix†

Shu-Qing Lv,[a] Wei Xu,[bc] Wujisiguleng Huang,[a] Guo-Cheng Lv*[b]
and Guang-Sheng Wang *[c]

Received 18th February 2019
Accepted 11th April 2019

DOI: 10.1039/c9ra01248f

rsc.li/rsc-advances

One-dimensional K–MnO$_2$ nanorods were prepared by a wet chemical process. Dopamine hydrochloride (PDA) layers with various thicknesses were coated and finally, the composites were filled in a poly(vinylidene fluoride) (PVDF) matrix using the hot-molding procedure. The complex permittivity and permeability of the K–MnO$_2$@PDA/PVDF composites could be adjusted by reactant amount ratios and filler contents. The minimum reflection loss could reach −49.4 dB and an effective absorption bandwidth (<−10 dB) covering 11.12 GHz was achieved with 20% filler content when the reactant amount ratio between K–MnO$_2$ and PDA was 4 : 0.375, which was derived from effective internal polarization processes. It is expected that these novel composites can be used as high-performance microwave absorbers.

Introduction

Due to the extensive use of electromagnetic waves in the GHz frequency range employed in electronic instruments and in telecommunication and related technologies in recent years, the materials of electromagnetic (EM) interference attenuation have attracted increasing attention owing to their clear use in eliminating undesirable EM radiation.[1,2] Compared to the research on conventional metals, many researches have been devoted to develop high-performance microwave absorption materials in the submicron or nanometer scales with the advantages of strong absorption, a wide absorption bandwidth, thinness, and lightweight to block harmful EM waves and convert EM energy into thermal energy through internal loss.[3–6]

Until now, diverse structures such as hollow,[7,8] porous,[9] foamed,[10] core–shell[11] and yolk–shell[12] structures have been investigated to achieve high-performance absorption. Among them, the synthesis of one-dimensional (1D) nanomaterials is an effective way to improve electromagnetic performance.[13–15] The large anisotropy of 1D nanomaterials may overcome the drawbacks of low permeability values at a high frequency due to the Snoek's limit,[16] which can greatly enhance the electromagnetic properties. Recent research has demonstrated that the absorbers with 1D nanostructures can achieve better absorption performance. For instance, Fe nanochains were prepared by Zhan *et al.* using a chemical route,[17] and the products achieved minimum reflection loss of −20.4 dB for a thickness of 2 mm. Yan *et al.*[18] reported Fe$_3$O$_4$ nanowires fabricated *via* an NaAc-assisted coprecipitation method that achieved a minimum reflection loss of −16.67 dB at 8.32 GHz.

Moreover, MnO$_2$ has gained wide attention in the field of shielding and absorption in the microwave band range due to its distinctive physical and chemical properties.[19–22] The structure of K–MnO$_2$ is constructed from edge-sharing double chains of MnO$_6$ octahedra, forming a 2 × 2 tunnel structure that can allow potassium insertion, improving its dielectric properties.[23,24]

Herein, we report a binary composite synthesized simply by 1D K–MnO$_2$ nanorods and polydopamine (PDA). The microwave absorption properties of the composite were researched systematically and showed a large absorption bandwidth in the GHz range. Therefore, this composite with a unique structure is a promising candidate for high-performance microwave absorption.

Experimental section

Preparation of K–MnO$_2$ nanorods

The K–MnO$_2$ nanorods were prepared by a hydrothermal method as outlined in our previous work.[25] Briefly, 0.01 mol KMnO$_4$ and 0.015 mol MnSO$_4$·H$_2$O were dissolved in 50 mL water with vigorous stirring at room temperature for 30 min. The dark brown precipitates were transferred into a Teflon-lined stainless autoclave after aging and kept at 150 °C for 24 h. After the reaction, the precipitates were centrifuged, washed, and dried for further characterization.

---

[a] School of Civil Engineering, Northeast Dianli University, Jilin 132012, PR China

[b] School of Materials Science and Technology, China University of Geosciences, Beijing, 100083, PR China. E-mail: guochenglv@cugb.edu.cn

[c] School of Chemistry, Beihang University, Beijing 100191, PR China. E-mail: wanggsh@buaa.edu.cn

† Electronic supplementary information (ESI) available. See DOI: 10.1039/c9ra01248f

Preparation of K–MnO$_2$@PDA nanofibers

The as-prepared K–MnO$_2$ nanorods (40 mg) were dispersed into 100 mL Tris buffer aqueous solution (2 mg mL^{-1}, pH 8.5) followed by the addition of dopamine hydrochloride (30 mg). After that, the reaction solution was stirred gently at room temperature for 20 min to form a uniform PDA coating. The K–MnO$_2$@PDA nanofibers were obtained by centrifugation and washed with deionized water. Meanwhile, samples were also prepared with 0, 3.75, 7.5, and 15 mg dopamine hydrochloride addition.

Preparation of K–MnO$_2$@PDA/PVDF nanocomposites

The desired amount of PVDF was dispersed in 25 mL of *N*,*N*-dimethylformamide (DMF) with magnetic stirring at room temperature for 30 min. Various amounts of K–MnO$_2$@PDA nanofibers were added and the solution became transparent. After stirring and ultrasonication for 1 h, the mixture was poured onto a glass plate to form a thin film and dried at 60 °C for 5 h. The dried mixture was pressed into cylinder-shaped samples ($\Phi_{\text{out}} = 7.00$ mm and $\Phi_{\text{in}} = 3.04$ mm) by hot pressing at 210 °C (Scheme 1). In the range of 2–18 GHz and with the coaxial wire method, we measured the complex permittivity and permeability values.

Physicochemical characterization of samples

The morphology and size of the K–MnO$_2$ nanorods and K–MnO$_2$@PDA nanofibers were examined using field emission scanning electron microscopy (FESEM, JSM-6700F) and high-resolution transmission electron microscopy (HR-TEM, JEOL JEM-2010F). Powder diffraction data were collected using an X-ray diffractometer (XRD, Philips X'Pert Pro Super). Thermogravimetric analysis (TG) was performed in N$_2$ using a Pyris Diamond TG analyzer (PerkinElmer Inc., USA). The samples were heated from 30 °C to 800 °C at a heating rate of 5 °C min^{-1}. The EM parameters were measured using a two-port vector network analyzer (Agilent E5071C).

Results and discussion

The structural characterizations of K–MnO$_2$ and K–MnO$_2$@PDA were carried out by SEM and TEM. The typical images of the samples display nanorod and nanofiber morphologies with diameters of about 30–50 nm and lengths of 0.5–5 μm. The typical powder XRD patterns of the as-synthesized products are shown in Fig. 1(e). It can be concluded that the diffraction peaks are uniquely indexed to the pure tetragonal phase of K–MnO$_2$ (JCPDS No. 42-1348) and no characteristic peaks for impurities are observed, suggesting its high purity and crystallinity. The strong diffraction peaks for K–MnO$_2$ and K–MnO$_2$@PDA are almost coincident; however, the intensities decrease due to the outer layer amorphous PDA. As shown in Fig. 1(f), the TG curve of K–MnO$_2$ exhibits three characteristic stepwise weight losses. The slight mass loss below 250 °C results from the loss of absorbed water and surface-related water. The rapid mass loss between 250 °C and 700 °C may be attributed to the loss of the water bound inside the 2 × 2 tunnels, the internal structural water and oxygen atoms on the surfaces; this indicates that the octahedral bond of MnO$_6$ begins to break and the tunnel structure also collapses to a certain extent. The evolution of the lattice oxygen is likely the reason for the final mass loss, which may lead to a phase change. On the basis of the weight loss rate, the amount of PDA in the composites is determined to be about 20 wt%. Moreover, we can observe from Fig. 2 that different PDA coating thicknesses can be achieved by controlling the reactant amount ratios, leading to the adjustment of the impedance matching condition by balancing the complex permittivity and permeability.

To investigate the electromagnetic wave absorption properties of K–MnO$_2$ nanorods and K–MnO$_2$@PDA nanofibers, products with various reactant amount ratios were blended with PVDF to form composites *via* a hot-press process. The frequency dependences relative permittivity and permeability, dielectric loss, and magnetic loss for several samples are shown in Fig. S1.† The real part of permittivity (ε') and real permeability (μ') represent the storage capability of the electric and magnetic energies, whereas

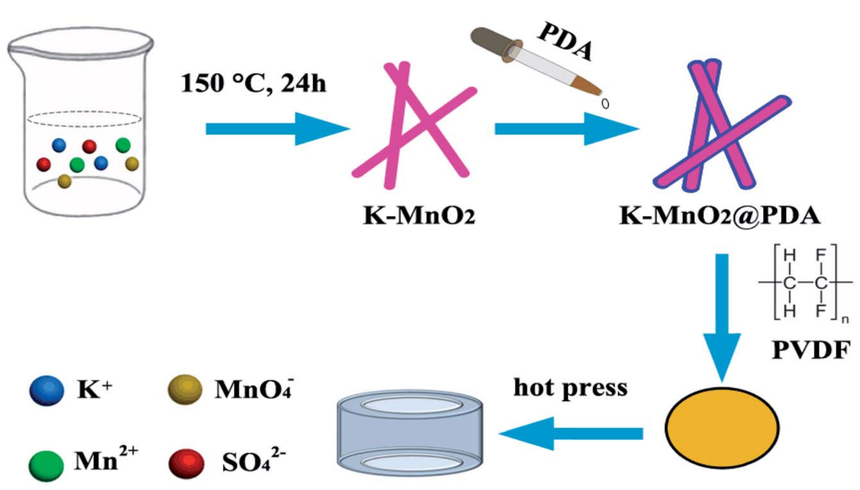

Scheme 1 Simplified illustration for the synthetic procedure of K–MnO$_2$@PDA/PVDF composites.

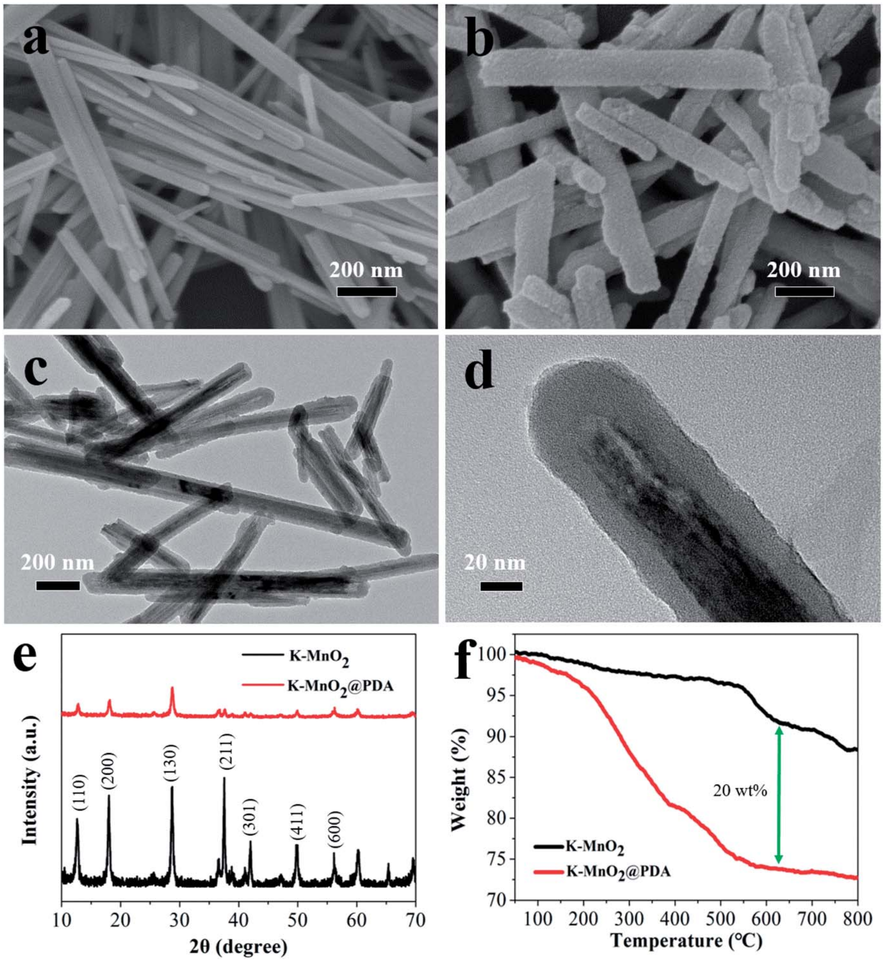

Fig. 1 SEM images of (a) K–MnO$_2$ nanorods and (b) K–MnO$_2$@PDA nanofibers. TEM images of (c and d) K–MnO$_2$@PDA, (e) XRD patterns and (f) TG curves.

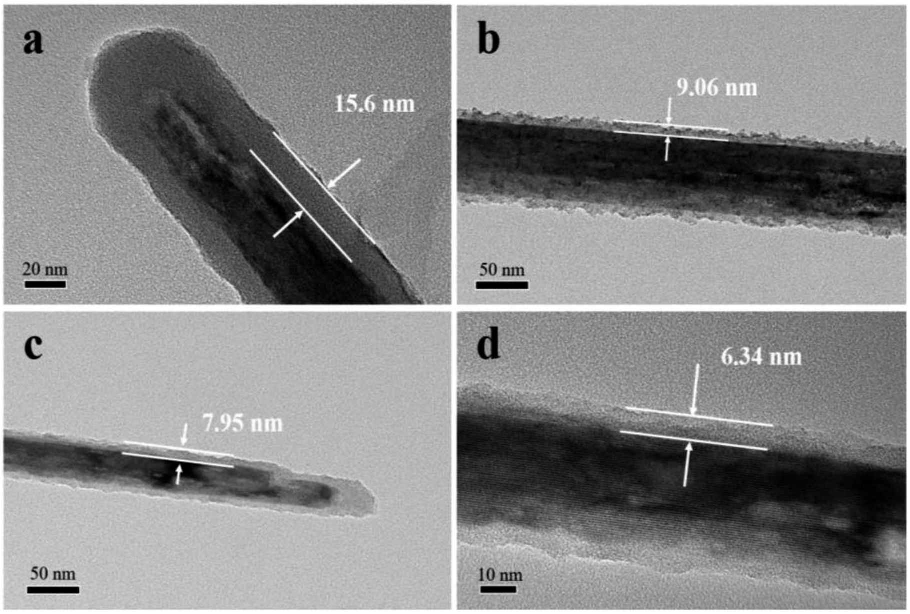

Fig. 2 TEM images of K–MnO$_2$@PDA nanofibers with various reactant amount ratios of (a) 4 : 3, (b) 4 : 1.5, (c) 4 : 0.75, (d) 4 : 0.375.

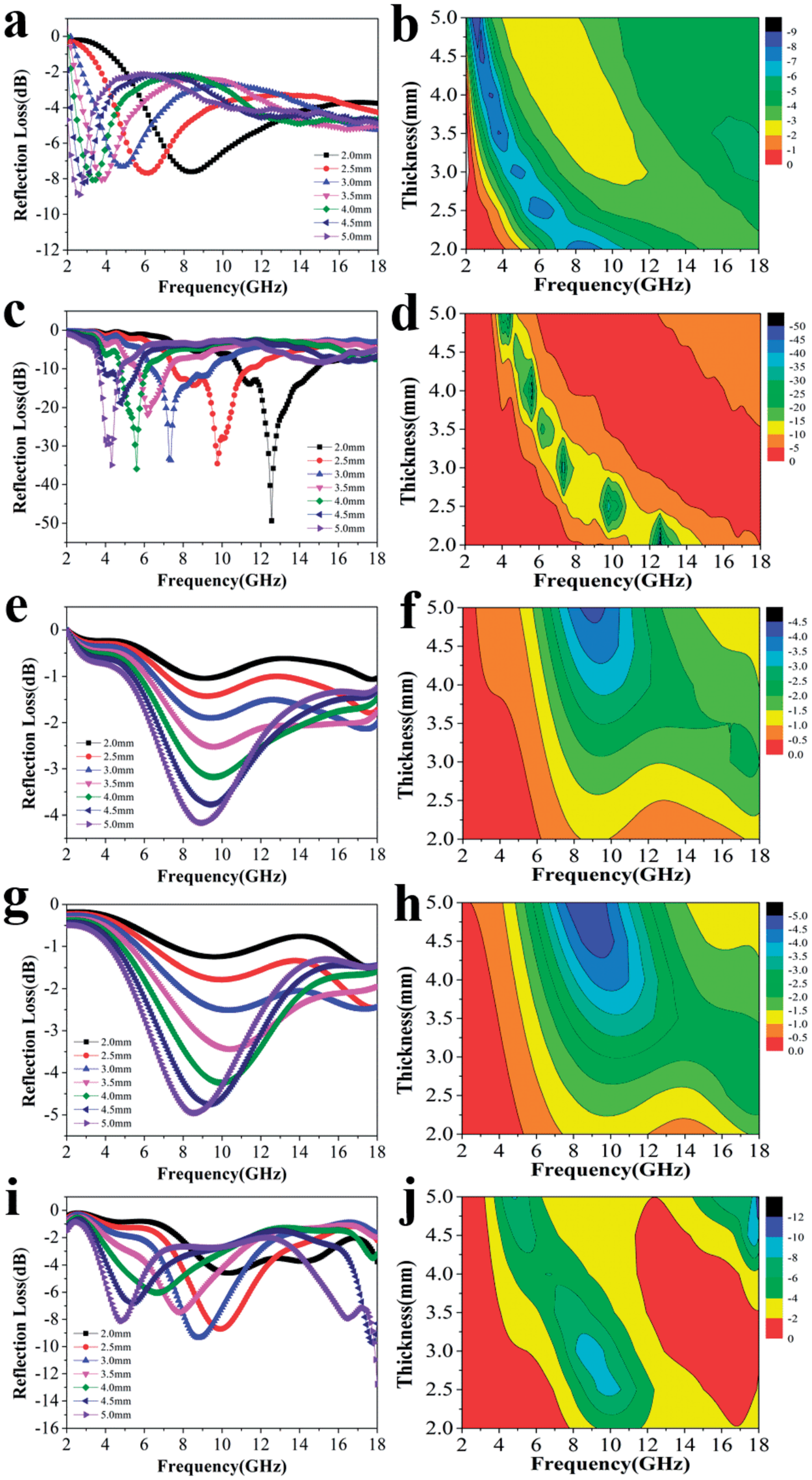

Fig. 3 The RL curves for nanofibers with various reactant amount ratios of (a) 4 : 0, (c) 4 : 0.375, (e) 4 : 0.75, (g) 4 : 1.5, (i) 4 : 3 and the corresponding color filled versions of RL (b, d, f, h, j).

imaginary permittivity (ε'') and imaginary permeability (μ'') are related to the dissipation of energy and magnetic loss, respectively.[26,27] It is worth mentioning that the values of ε' and ε'' tend to decrease after gradual increase in the amounts of PDA. Negative values of μ'' appear in the high frequency range, which may be caused by the electromagnetic field-induced eddy current, suggesting that the magnetic energy is radiated out.[28]

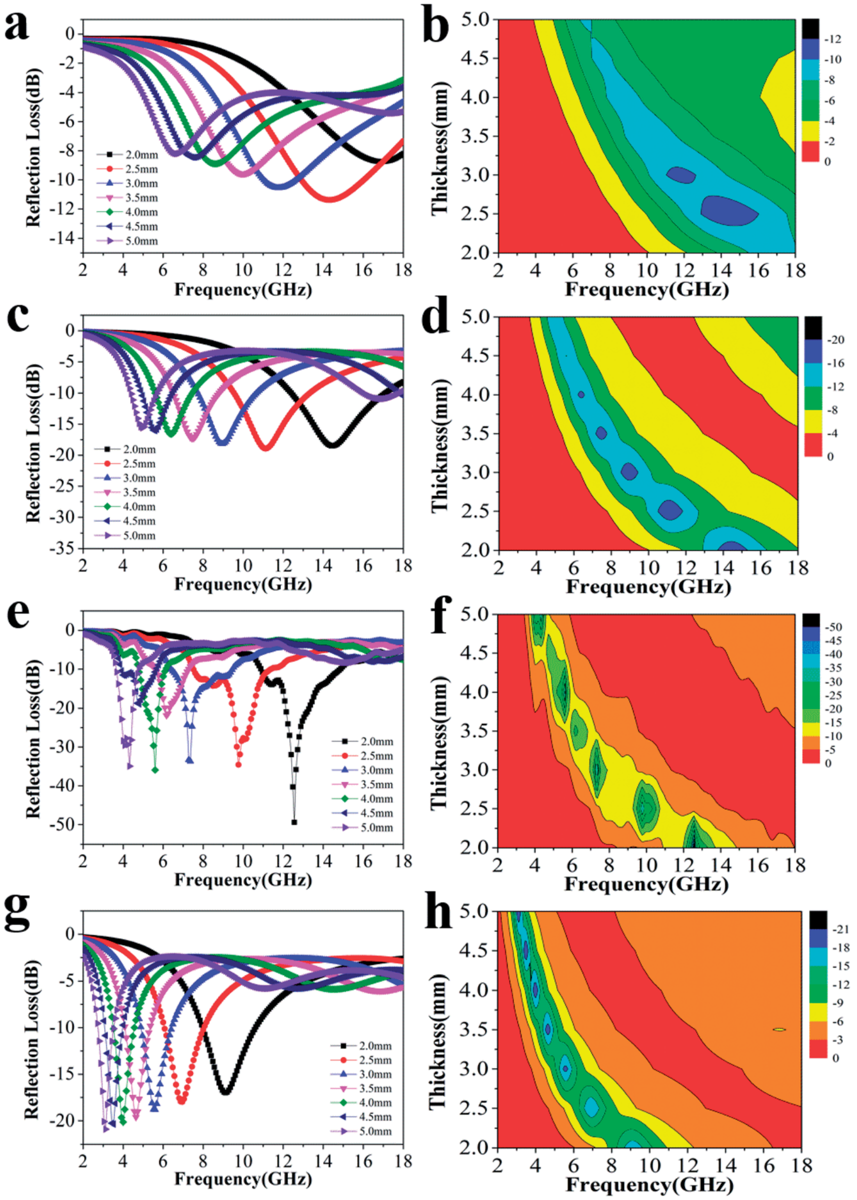

Fig. 4 The RL curves for nanofibers with (a) 5%, (c) 10%, (e) 20%, (g) 30% filler contents with thicknesses of 2.0–5.0 mm, and the corresponding color filled versions of RL (b, d, f, h).

The reflection loss (RL) values can be calculated according to the measured relative permittivity and permeability for a given frequency range and layer thickness based on the transmission line theory using the following equation:[29,30]

$$R = 20\log\left|\frac{Z_{\text{in}}-1}{Z_{\text{in}}+1}\right| \tag{1}$$

$$Z_{\text{in}} = \sqrt{\frac{\mu_r}{\varepsilon_r}}\tanh\left[j\left(\frac{2f\pi d}{c}\right)\sqrt{\mu_r\varepsilon_r}\right] \tag{2}$$

Here, Z_{in} is the normalized input characteristic impedance, and ε_r and μ_r are the complex permittivity and permeability of the composite absorber, respectively; d is the thickness of the absorber, f is the frequency, and c is the velocity of light in free space.

Fig. 3 shows the RL curves and corresponding color versions of the five samples with different ratios at layer thickness of 2.0–5.0 mm in the range of 2–18 GHz. It is well-known that the key

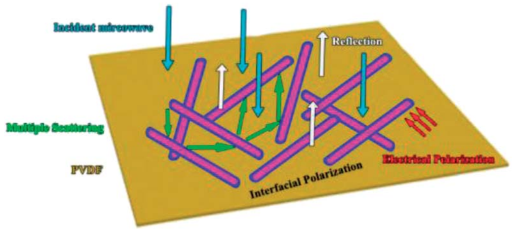

Scheme 2 Illustration of possible microwave absorbing mechanisms of the K–MnO_2@PDA/PVDF composites.

factors for measuring the absorption properties of a material are mainly the RL values and effective frequency bandwidth (RL < -10 dB). We can observe that the reactant amount ratios have an important influence on the absorption properties. Compared with other amount ratios, for 4 : 0.375 of reactants, the minimum RL value can reach −49.4 dB at 12.56 GHz with a low layer thickness of 2.0 mm; the effective frequency bandwidth is from 10.96 to 14.8 GHz (3.84 GHz). Meanwhile, at layer thickness of 2.0–5.0 mm, the bandwidth is from 3.68 to 14.8 GHz (11.12 GHz), which is more than half of the test bandwidth.

As a typical kind of dielectric and multi-interfacial material, the dielectric loss mechanism of K–MnO$_2$@PDA/PVDF is mainly attributed to polarization processes such as electrical polarization, interfacial polarization, and multiple scattering. Each polarization process results in a profound effect on the loss of energy. At a low frequency, the Debye dipolar relaxation is the main cause of dielectric loss in the composites.[31] On the basis of the Debye theory, ε' and ε'' can be described as follows:[32,33]

$$\varepsilon' = \varepsilon_\infty + \frac{\varepsilon_s - \varepsilon_\infty}{1 + (2\pi f)^2 \tau^2} \tag{3}$$

$$\varepsilon'' = \frac{2\pi f \tau (\varepsilon_s - \varepsilon_\infty)}{1 + (2\pi f)^2 \tau^2} \tag{4}$$

Here, f, ε_s, ε_∞, and τ are the frequency, static permittivity, relative dielectric permittivity at the high frequency limit, and polarization relaxation time, respectively.

According to the above-mentioned information, the relationship between ε' and ε'' can be described as follows:[34]

$$\left(\varepsilon' - \frac{\varepsilon_s - \varepsilon_\infty}{2}\right)^2 + (\varepsilon'')^2 = \left(\frac{\varepsilon_s - \varepsilon_\infty}{2}\right)^2 \tag{5}$$

Thus, the plot of ε' *versus* ε'' would be a single semicircle, which is generally denoted as the Cole–Cole semicircle. Each semicircle corresponds to an effective Debye dipolar relaxation process.[35] It can be observed that Fig. S2c† exhibits the most semicircles among all. This confirms that K–MnO$_2$@PDA with a reactant ratio of 4 : 0.375 has the most excellent microwave absorption properties.

To explore the absorption properties for different loadings, we also tested four samples with 5%, 10%, 20%, and 30% filler contents at a ratio of 4 : 0.375, and their RL values are presented in Fig. 4. Except for the observations for 20% filler content, the absorption properties for other three filler contents were also favorable as a whole. The minimum RL values and effective frequency bandwidths for 5%, 10%, and 30% filler contents over 2–18 GHz were −11.4 dB, 4.96 GHz; −18.9 dB, 12.64 GHz and −20.9 dB, 7.76 GHz, respectively. Furthermore, Fig. S4† displays that all the ε' and ε'' values increase dramatically after the introduction of more fillers, indicating that the composite can significantly improve the polarization ability and the dielectric-loss capability. Additionally, all the ε' curves show a decreasing trend with increasing frequency, which is indicative of a frequency dispersion behavior. This can be explained by the increased lag in polarization with respect to the electric-field change at a higher frequency.[36] This decreasing trend also occurs in the case of ε'' (Scheme 2).

The attenuation constant α determines the attenuation properties of materials and can be expressed as follows:[37]

$$\alpha = \frac{\sqrt{2}\pi f}{c} \times \sqrt{(\mu''\varepsilon'' - \mu'\varepsilon') + \sqrt{(\mu''\varepsilon'' - \mu'\varepsilon')^2 + (\mu'\varepsilon'' + \mu''\varepsilon')^2}} \tag{6}$$

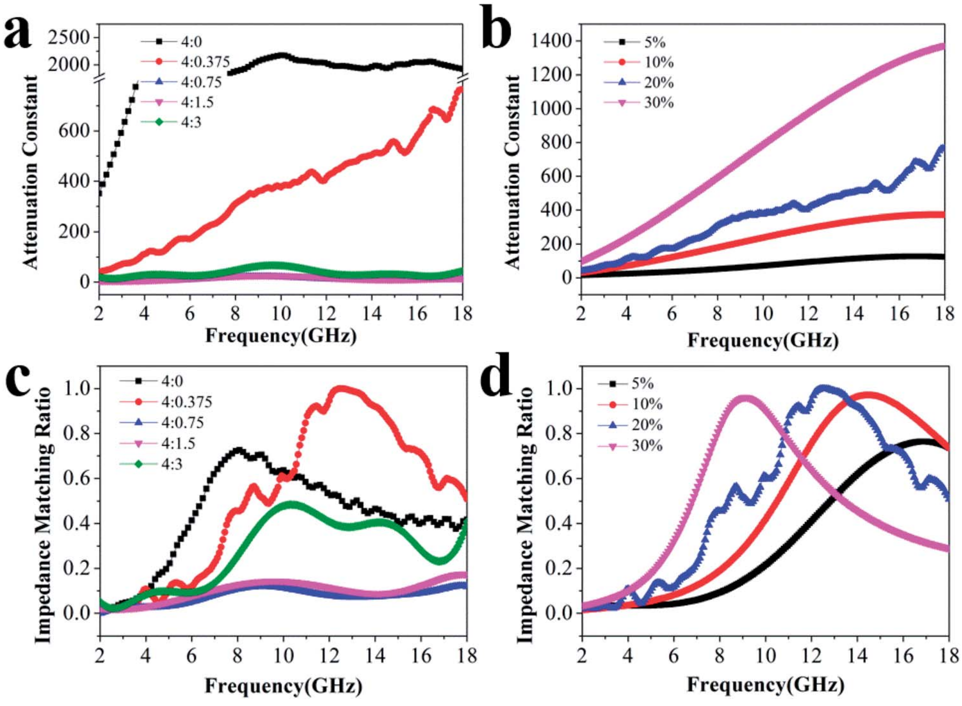

Fig. 5 Attenuation constant α (a) of different reactant amount ratios with 20% filler content and (b) those of various filler contents at the ratio of 4 : 0.375; the corresponding impedance matching ratios (c and d).

Here, f is the frequency of the electromagnetic wave and c is the velocity of light in vacuum. As shown in Fig. 5(a) and (b), the attenuation constants of composites with different reactant amount ratios increase with decreasing proportion of PDA and also increase with higher filler contents. The larger attenuation constant results in more dielectric loss, which is consistent with the variation in each permittivity. However, regardless of whether the attenuation constant is higher or lower, better microwave absorption performance is not always obtained. This is due to the consideration of the offset and balance between the impedance matching ratio and the attenuation constant. Generally, the microwave absorption properties are primarily determined by the impedance matching performance, indicating the efficient complementarities between the magnetic loss and dielectric loss.[38] It can be observed from Fig. 5(c) and (d) that the impedance matching ratio of the sample with a reactant amount ratio of 4 : 0.375 moves closer to 1.0. The sample with 20% filler content also presents a moderate ratio compared to the others, revealing that microwaves are effectively reduced after entering the absorber.

Conclusions

In summary, K–MnO_2@PDA composites with various coating thicknesses were synthesized successfully by adjusting the reactant amount ratios. The hybrid showed excellent absorption strength with a maximum absorption peak of −49.4 dB and an effective absorption bandwidth of 11.12 GHz with 20% filler content when the reactant amount ratio was 4 : 0.375. The microwave absorption properties of the composites with different filler contents (5%, 10%, 20%, and 30%) at a reactant ratio of 4 : 0.375 were also researched in detail. The above results verified that the hybrids can achieve considerable electromagnetic wave absorption performance. This was attributed to the internal polarization process resulting from the successful regulation of reactant amount ratios and filler loading. It is believed that K–MnO_2@PDA has great potential for use in the microwave absorption application field.

Conflicts of interest

There are no conflicts to declare.

Acknowledgements

This work was supported by the National Natural Science Foundation of China (No. 51472012), the Fundamental Research Funds for the Central Universities.

Notes and references

1 X.-M. Meng, X.-J. Zhang, C. Lu, Y.-F. Pan and G.-S. Wang, *J. Mater. Chem. A*, 2014, **2**, 18725–18730.

2 Y.-F. Pan, G.-S. Wang, L. Liu, L. Guo and S.-H. Yu, *Nano Res.*, 2017, **10**, 284–294.

3 J. Feng, F. Pu, Z. Li, X. Li, X. Hu and J. Bai, *Carbon*, 2016, **104**, 214–225.

4 X. Li, J. Feng, H. Zhu, C. Qu, J. Bai and X. Zheng, *RSC Adv.*, 2014, **4**, 33619–33625.

5 Y. Sun, J. Zhang, Y. Zong, X. Deng, H. Zhao, J. Feng, M. He, X. Li, Y. Peng and X. Zheng, *ACS Appl. Mater. Interfaces*, 2019, **11**, 6374–6383.

6 X. Zheng, J. Feng, Y. Zong, H. Miao, X. Hu, J. Bai and X. Li, *J. Mater. Chem. C*, 2015, **3**, 4452–4463.

7 X.-J. Zhang, J.-Q. Zhu, P.-G. Yin, A.-P. Guo, A.-P. Huang, L. Guo and G.-S. Wang, *Adv. Funct. Mater.*, 2018, **28**, 1800761.

8 G. Wang, Z. Gao, S. Tang, C. Chen, F. Duan, S. Zhao, S. Lin, Y. Feng, L. Zhou and Y. Qin, *ACS Nano*, 2012, **6**, 11009–11017.

9 F. Ye, Q. Song, Z. Zhang, W. Li, S. Zhang, X. Yin, Y. Zhou, H. Tao, Y. Liu, L. Cheng, L. Zhang and H. Li, *Adv. Funct. Mater.*, 2018, **28**, 1707205.

10 Y. Zhang, Y. Huang, T. Zhang, H. Chang, P. Xiao, H. Chen, Z. Huang and Y. Chen, *Adv. Mater.*, 2015, **27**, 2049–2053.

11 Q. Liu, Q. Cao, H. Bi, C. Liang, K. Yuan, W. She, Y. Yang and R. Che, *Adv. Mater.*, 2016, **28**, 486–490.

12 J. Liu, J. Cheng, R. Che, J. Xu, M. Liu and Z. Liu, *J. Phys. Chem. C*, 2013, **117**, 489–495.

13 X. Liu, Y. Chen, X. Cui, M. Zeng, R. Yu and G.-S. Wang, *J. Mater. Chem. A*, 2015, **3**, 12197–12204.

14 S.-Q. Lv, Y.-F. Pan, P.-B. Yang and G.-S. Wang, *RSC Adv.*, 2016, **6**, 55546–55551.

15 W. Xu, Y.-F. Pan, W. Wei, G.-S. Wang and P. Qu, *Appl. Surf. Sci.*, 2018, **428**, 54–60.

16 G. Chai, D. Xue, X. Fan, X. Li and D. Guo, *Appl. Phys. Lett.*, 2008, **93**, 152516.

17 X. Zhan, H. Tang, Y. Du, A. Talbi, J. Zha and J. He, *RSC Adv.*, 2013, **3**, 15966–15970.

18 A. Yan, Y. Liu, Y. Liu, X. Li, Z. Lei and P. Liu, *Mater. Lett.*, 2012, **68**, 402–405.

19 G.-S. Wang, S. He, X. Luo, B. Wen, M.-M. Lu, L. Guo and M.-S. Cao, *RSC Adv.*, 2013, **3**, 18009–18015.

20 R. Koivula, J. Pakarinen, M. Sivenius, K. Sirola, R. Harjula and E. Paatero, *Sep. Purif. Technol.*, 2009, **70**, 53–57.

21 X. Wang, L. Mei, X. Xing, L. Liao, G. Lv, Z. Li and L. Wu, *Appl. Catal., B*, 2014, **160–161**, 211–216.

22 J. Tao, K. Song, G. Lv, L. Mei, Z. Li, L. Liao, X. Wang, X. Xing and B. Xu, *Mater. Express*, 2014, **4**, 539–544.

23 L. Athouël, P. Arcidiacono, C. Ramirez-Castro, O. Crosnier, C. Hamel, Y. Dandeville, P. Guillemet, Y. Scudeller, D. Guay, D. Bélanger and T. Brousse, *Electrochim. Acta*, 2012, **86**, 268–276.

24 L. Kang, M. Zhang, Z.-H. Liu and K. Ooi, *Spectrochim. Acta, Part A*, 2007, **67**, 864–869.

25 W. Xu, G. Lv, X. Xing, X.-J. Zhang and G.-S. Wang, *Sci. Adv. Mater.*, 2016, **8**, 966–971.

26 X.-J. Zhang, G.-S. Wang, W.-Q. Cao, Y.-Z. Wei, J.-F. Liang, L. Guo and M.-S. Cao, *ACS Appl. Mater. Interfaces*, 2014, **6**, 7471–7478.

27 C. Tian, Y. Du, P. Xu, R. Qiang, Y. Wang, D. Ding, J. Xue, J. Ma, H. Zhao and X. Han, *ACS Appl. Mater. Interfaces*, 2015, **7**, 20090–20099.

28 M. Zhang, G. Zhangzhu, S. Wen, H. Lu, R. Wang, W. Li, S. Ding, A. Ghulam and P. Zheng, *Chem. Eng. J.*, 2018, **345**, 345–352.

29 X. Jian, B. Wu, Y. Wei, S. X. Dou, X. Wang, W. He and N. Mahmood, *ACS Appl. Mater. Interfaces*, 2016, **8**, 6101–6109.

30 Y.-F. Pan, G.-S. Wang and Y.-H. Yue, *RSC Adv.*, 2015, **5**, 71718–71723.

31 M.-S. Cao, W.-L. Song, Z.-L. Hou, B. Wen and J. Yuan, *Carbon*, 2010, **48**, 788–796.

32 W. Xu, G.-S. Wang and P.-G. Yin, *Carbon*, 2018, **139**, 759–767.

33 H. Yu, T. Wang, B. Wen, M. Lu, Z. Xu, C. Zhu, Y. Chen, X. Xue, C. Sun and M. Cao, *J. Mater. Chem.*, 2012, **22**, 21679–21685.

34 G.-S. Wang, X.-J. Zhang, Y.-Z. Wei, S. He, L. Guo and M.-S. Cao, *J. Mater. Chem. A*, 2013, **1**, 7031–7036.

35 S. He, G.-S. Wang, C. Lu, J. Liu, B. Wen, H. Liu, L. Guo and M.-S. Cao, *J. Mater. Chem. A*, 2013, **1**, 4685–4692.

36 H. Wang, Y. Y. Dai, D. Y. Geng, S. Ma, D. Li, J. An, J. He, W. Liu and Z. D. Zhang, *Nanoscale*, 2015, **7**, 17312–17319.

37 D. Ding, Y. Wang, X. Li, R. Qiang, P. Xu, W. Chu, X. Han and Y. Du, *Carbon*, 2017, **111**, 722–732.

38 Z. Li, X. Li, Y. Zong, G. Tan, Y. Sun, Y. Lan, M. He, Z. Ren and X. Zheng, *Carbon*, 2017, **115**, 493–502.